

## Continuous tuning of compensated ferrimagnetism in $\text{Gd}_{3-x}\text{Ho}_x\text{Fe}_5\text{O}_{12}$ thin films

Hao Bai,<sup>1,\*</sup> Wenlong Si,<sup>2,\*</sup> Heng-An Zhou,<sup>1,\*</sup> Ledong Wang,<sup>1</sup> Teng Xu,<sup>1</sup> Yiqing Dong,<sup>1</sup> Jing Zhu,<sup>2,†</sup> and Wanjun Jiang<sup>1,‡</sup>  
<sup>1</sup>State Key Laboratory of Low-Dimensional Quantum Physics, Department of Physics, and Frontier Science Center for Quantum Information, Tsinghua University, Beijing 100084, China

<sup>2</sup>Key Laboratory of Advanced Materials (MOE), School of Materials Science and Engineering, Tsinghua University, Beijing 100084, China



(Received 12 February 2023; revised 3 July 2023; accepted 7 August 2023; published 6 September 2023)

Rare-earth iron garnets (ReIGs) are attracting considerable attention because they could enable many intriguing spintronic phenomena. Material choices of these garnets are, however, limited to rather simple compositions, such as  $\text{Y}_3\text{Fe}_5\text{O}_{12}$ ,  $\text{Tm}_3\text{Fe}_5\text{O}_{12}$ , and  $\text{Gd}_3\text{Fe}_5\text{O}_{12}$ , among many others. The magnetic properties of these garnets, including saturation magnetization, anisotropy, and damping parameter, are accordingly limited within a narrow parameter space. In this study, we will first grow a series of substituted ReIGs of composition  $\text{Gd}_{3-x}\text{Ho}_x\text{Fe}_5\text{O}_{12}$  ( $x_{\text{Ho}} = 0-3$ ). Subsequently, a continuous tuning of magnetic parameters, including the net saturation magnetization ( $M_S$ ), the magnetization compensation temperature ( $T_M$ ), and the damping parameter ( $\alpha$ ), are also demonstrated through linearly changing the Ho concentration. The present method could be useful for designing garnets with desired material parameters, which could be incorporated for enabling unique spintronic devices based on compensated ReIGs.

DOI: [10.1103/PhysRevMaterials.7.094401](https://doi.org/10.1103/PhysRevMaterials.7.094401)

### I. INTRODUCTION

Rare-earth iron garnets (ReIG) of composition  $\text{Re}_3\text{Fe}_5\text{O}_{12}$  are typical ferrimagnetic insulators, which have attracted substantial interest in the spintronics community [1–11]. For example, long-distance magnon transmission [12,13], efficient perpendicular magnetization [5,10,14–22], and other intriguing spin-orbit physics have been reported in these garnets [23,24]. Due to their different temperature-dependent magnetizations of the  $\text{Fe}^{3+}$  and  $\text{Re}^{3+}$  sublattices [3,4,25,26], compensated ferrimagnetism with either a zero net magnetization or a zero angular momentum could occur. The former is termed as the magnetization compensation temperature ( $T_M$ ) and the latter is termed as the angular momentum compensation temperature ( $T_A$ ). Around these characteristic temperatures, the efficient spin-orbital torque (SOT) switching [27–30] and the ultrafast domain wall motion [31,32] have been reported. Note that similar behaviors have also been reported in metallic compensated ferrimagnets [33–41]. However, the ranges of these characteristic temperatures ( $T_M$  and  $T_A$ ), together with other key material-specific parameters are scattered and difficult to tune to desired values, since they are intrinsically determined by ratios and choices of the Re and Fe elements. For example, several different compensated garnets with determined characteristic temperatures have been explored including GdIG [3,4,28,42–45], TbIG [18,27,29], DyIG [21], and HoIG [46]. In this regard, it is important to explore an effective method for designing compensated ferrimagnets with desired parameters that could cover a

wider range. This is essential to fulfill the varied application situations.

Meanwhile, the damping parameters ( $\alpha$ ) of these ReIGs are drastically different. For example,  $\alpha$  on the order of  $10^{-4}$  in LuIG [9],  $10^{-3} - 10^{-2}$  in TmIG [11],  $10^{-1}$  in DyIG [21], and  $10^{-3}$  in EuIG [19] have been reported. It is also intriguing to continuously tune the damping parameters of garnets. Additionally, a perpendicular magnetic anisotropy (PMA) is required for the spin-orbitronic applications of ReIGs [Re = Tb [5,18,19,29], Sm [14,47], Tm [15,17], Y [16,48], Eu [19,20], Dy [21], Gd [28,43], and Ho [46]]. Since garnet films are typically made on single-crystalline substrates, it is interesting to explore the evolution of PMA as a function of lattice mismatch. These important aspects will be explored in this work.

In the present study, we choose two representative ferrimagnets,  $\text{Gd}_3\text{Fe}_5\text{O}_{12}$  and  $\text{Ho}_3\text{Fe}_5\text{O}_{12}$ , to show a continuous tuning of compensated ferrimagnetism. In particular, various garnet films of composition  $\text{Gd}_{3-x}\text{Ho}_x\text{Fe}_5\text{O}_{12}$  ( $x_{\text{Ho}} = 0, 0.75, 1, 1.5, 2, 2.25, 3$ ) will be synthesized by the cosputtering method. The evolution of magnetic properties as a function of the Ho concentrations ( $x_{\text{Ho}}$ ), including the net saturation magnetization ( $M_S$ ), magnetization compensation temperature ( $T_M$ ), and damping parameter ( $\alpha$ ), will be subsequently studied. By invoking the molecular-field theory (MFT), their dependences will be explained.

### II. EXPERIMENT

Based on our early experience of growing  $\text{Gd}_3\text{Fe}_5\text{O}_{12}$  films [43], the  $\text{Gd}_{3-x}\text{Ho}_x\text{Fe}_5\text{O}_{12}$  ( $\text{Gd}_{3-x}\text{Ho}_x\text{IG}$ ) films with varied Ho concentrations ( $x_{\text{Ho}}$ ) will be synthesized. This is made possible by using an ultrahigh-vacuum (UHV) sputtering system that is equipped with cosputtering mode and

\*These authors contributed equally to this work.

†jzhu@mail.tsinghua.edu.cn

‡jiang\_lab@tsinghua.edu.cn

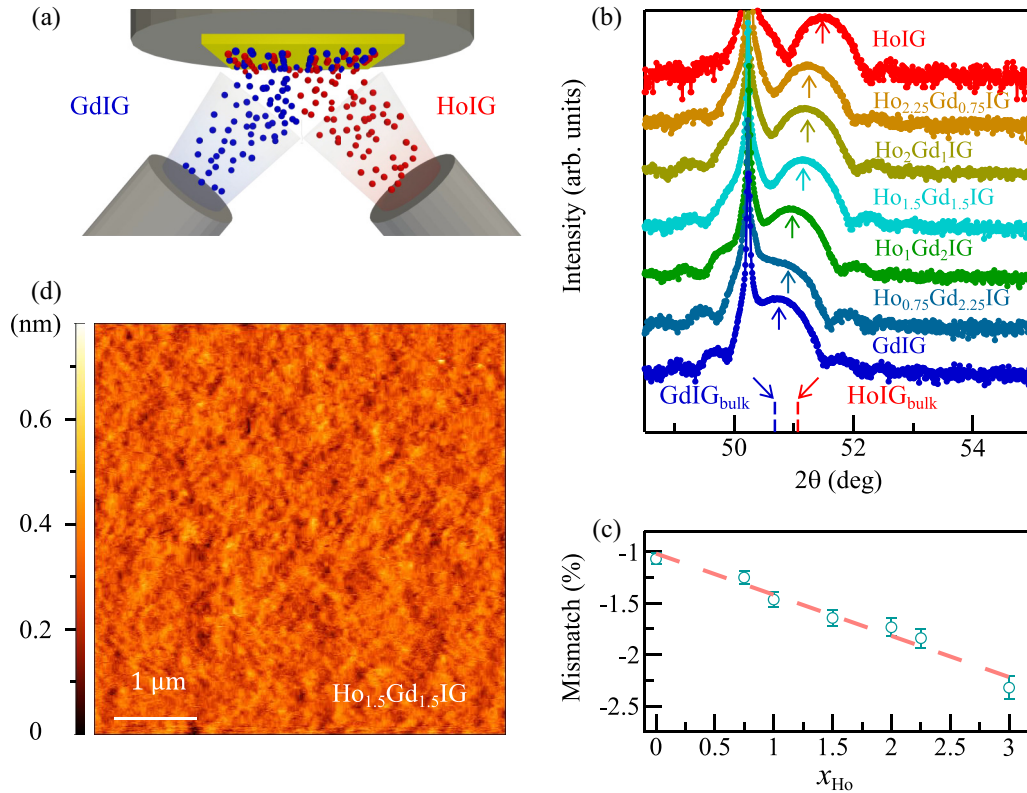


FIG. 1. (a) The schematic illustration of the cosputtering mode for synthesizing the  $\text{Gd}_{3-x}\text{Ho}_x\text{IG}$  films. (b) The XRD spectra of the  $\text{Gd}_{3-x}\text{Ho}_x\text{IG}$  films ( $x_{\text{Ho}} = 0, 0.75, 1, 1.5, 2, 2.25, 3$ ). The thickness is fixed at 13.7 nm. The dashed blue (red) line at  $2\theta = 50.68^\circ$  ( $51.07^\circ$ ) represents the diffraction peak of bulk GdIG (HoIG), respectively. (c) The evolution of the lattice mismatch between the  $\text{Gd}_{3-x}\text{Ho}_x\text{IG}$  films and the GSGG substrate, which is plotted against the Ho concentrations ( $x_{\text{Ho}}$ ). (d) The surface morphology of the  $\text{Gd}_{1.5}\text{Ho}_{1.5}\text{IG}$  film. The surface roughness within the scanning area is estimated to be less than 0.1 nm (rms).

two radio-frequency (RF) power supplies. In the cosputtering mode, the growth power of the  $\text{Gd}_3\text{Fe}_5\text{O}_{12}$  and  $\text{Ho}_3\text{Fe}_5\text{O}_{12}$  targets can be precisely adjusted, which enables continuous control of the relative composition of the  $\text{Gd}_{3-x}\text{Ho}_x\text{IG}$  films. In particular, substituted garnets of various compositions  $\text{Gd}_{3-x}\text{Ho}_x\text{IG}$  ( $x_{\text{Ho}} = 0, 0.75, 1, 1.5, 2, 2.25, 3$ ), but with a fixed thickness of 13.7 nm, were deposited on top of (111)-oriented  $\text{Gd}_3\text{Sc}_2\text{Ga}_3\text{O}_{12}$  (GSGG) single-crystalline substrates at  $700^\circ\text{C}$ . The base pressure of the main chamber is lower than  $1 \times 10^{-8}$  Torr and the Ar working pressure is 3 mTorr. *In situ* annealing for over 1 h was conducted in the same sputtering chamber at  $700^\circ\text{C}$  under a mixture of argon and oxygen environment, with an oxygen partial pressure of 20% at 1.5 mTorr. After annealing, all films were naturally cooled down to room temperature. For magnetotransport measurement, a 4 nm Pt layer was deposited on these  $\text{Gd}_{3-x}\text{Ho}_x\text{IG}$  (13.7 nm) films by using direct-current (DC) magnetron sputtering without breaking the vacuum.

The surface morphology was characterized by using atomic force microscopy (AFM). The crystal structure was characterized by using x-ray diffraction (XRD) and a scanning transmission electron microscope (STEM) which is equipped with high-angle annual dark-field (HAADF) imaging capability. The Gd and Ho concentrations were checked by using energy-dispersive x-ray spectroscopy (EDS). The magnetometry measurements were carried out by using a vibrating sample magnetometer (VSM), together with a

magnetic property measurement system (MPMS). Six-terminal Hall bar devices [ $20 \mu\text{m}$  (width)  $\times$   $120 \mu\text{m}$  (length)] were patterned for electrical transport studies. Damping parameters were obtained by conducting a spin-torque ferromagnetic resonance (STFMR) experiment using microstripe devices of dimension  $20 \mu\text{m}$  (width)  $\times$   $135 \mu\text{m}$  (length). During this measurement, static in-plane magnetic fields were swept at an angle of  $45^\circ$  with respect to the longitude direction ( $x$ ). A nominal power of 100 mW and varied frequencies of 5–8.5 GHz were applied using an amplitude-modulated microwave source.

### III. RESULTS AND DISCUSSION

#### A. Part I: Crystal structure of the $\text{Gd}_{3-x}\text{Ho}_x\text{IG}$ films

Shown in Fig. 1(a) is a schematic illustration of the cosputtering mode, in which the yellow cuboid represents the (111)-oriented single-crystalline GSGG substrate, and the blue and red spheres represent the GdIG and HoIG molecules, respectively. Various  $\text{Gd}_{3-x}\text{Ho}_x\text{IG}$  films with different Ho compositions ( $x_{\text{Ho}}$ ) can be obtained via accordingly adjusting growth powers, and hence growth rates of the two targets. These  $\text{Gd}_{3-x}\text{Ho}_x\text{IG}$  films were investigated by XRD, with their  $2\theta$  scan spectra being shown in Fig. 1(b). In addition to the sharp (444) peak ( $2\theta = 50.24^\circ$ ) from the GSGG substrate, it can be seen that all films exhibit (444) diffraction peaks without indication of a secondary phase. Compared

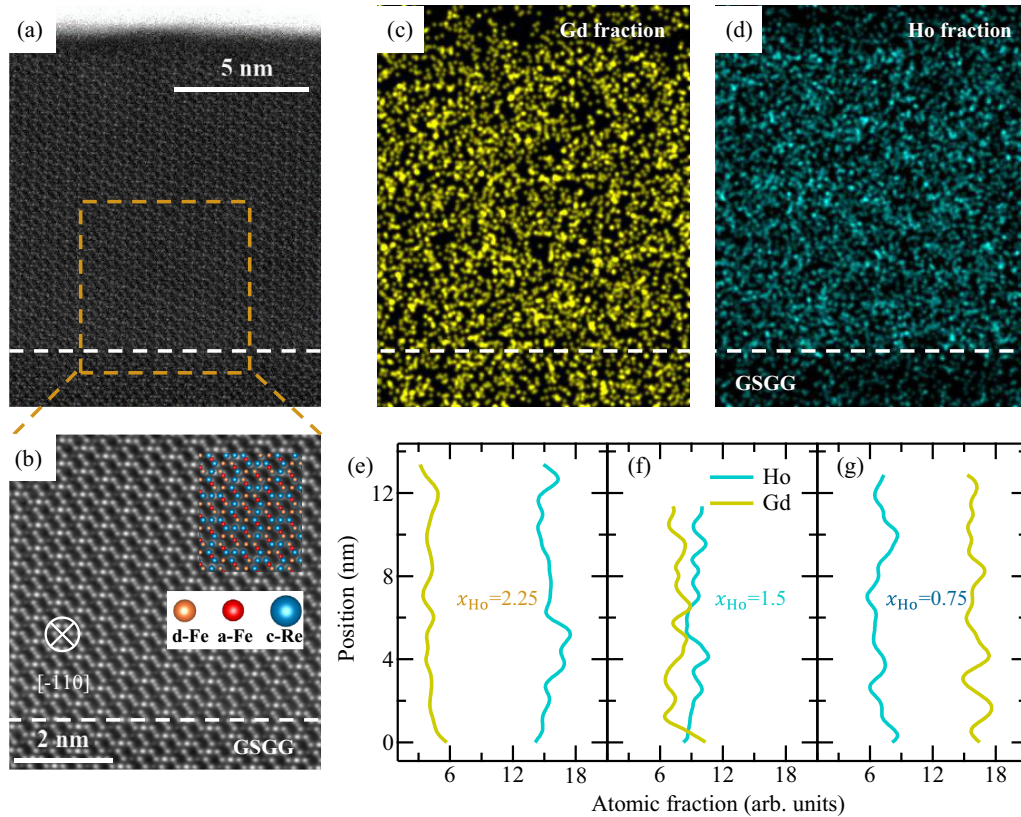


FIG. 2. (a) The corresponding HAADF image of the  $\text{Gd}_{2.25}\text{Ho}_{0.75}\text{IG}$  film. The scale bar is 5 nm. (b) The high-resolution HAADF image projected along the  $[-110]$  direction for the selected area in (a). The blue (red and yellow) spheres represent the Gd/Ho (a-Fe and d-Fe) elements, respectively. (c,d) The distribution of the Gd and Ho elements, where the yellow (blue) color represents the Gd and Ho elements, respectively. The whole area inside (a,c,d) denotes the line profile zone, which is used to quantitatively determine the relative atomic fraction between the Ho and Gd elements. (e–g) The relative atomic fraction of the Ho and Gd elements along the growth direction for the  $\text{Gd}_{3-x}\text{Ho}_x\text{IG}$  films with  $x_{\text{Ho}} = 2.25, 1.5,$  and  $0.75$ .

with the GSGG substrate, the larger angle of (444) peaks indicates the substrate-induced tensile strain. Furthermore, the increased position of diffraction peaks in GdIG (HoIG) films with respect to bulk GdIG (HoIG) samples [1,2,22,49,50] provides evidence of tensile strain. The peak of the bulk GdIG (HoIG) samples is indicated by the dashed blue (red) line in Fig. 1(b). The influence of tensile strain on the magnetic anisotropy will be discussed later [15,17,22]. Moreover, the corresponding angles of (444) peaks progressively increase with the increased Ho concentrations ( $x_{\text{Ho}}$ ), implying a continuous decrease of the lattice constant ( $a_{\text{film}}$ ) from 1.2437 nm at  $x_{\text{Ho}} = 0$  to 1.2279 nm at  $x_{\text{Ho}} = 3$ , which are calculated by using the Bragg equation. Quantitatively, the lattice mismatch ( $\varepsilon_{\text{mis}}$ ) can be computed as  $\varepsilon_{\text{mis}} = (a_{\text{film}} - a_{\text{sub}})/a_{\text{sub}}$ , with  $a_{\text{sub}} = 1.2571$  nm being the calculated lattice constant of the present GSGG substrate. Shown in Fig. 1(c) is a linear dependence of  $\varepsilon_{\text{mis}}$  on the Ho compositions ( $x_{\text{Ho}}$ ), which can be formulated as

$$\varepsilon_{\text{mis}}(x_{\text{Ho}}) = -1.0145 - k_{\text{mis}}x_{\text{Ho}}, \quad (1)$$

where  $\varepsilon_{\text{mis}}^{\text{GdIG}} = -1.0145$  is the lattice mismatch between the GdIG film and the GSGG substrate; the slope  $k_{\text{mis}} = 0.4018$  arises from the smaller radius of the  $\text{Ho}^{3+}$  ions.

Shown in Fig. 1(d) is the surface morphology of the  $\text{Gd}_{1.5}\text{Ho}_{1.5}\text{IG}$  film which was examined by AFM. A root mean

square (rms) roughness for a scanning area of  $5 \times 5 \mu\text{m}^2$  is found to be less than 0.1 nm. The high crystalline quality, the sharp interface, and the relative composition ratios of the Gd and Ho elements are examined by using STEM and EDS. Shown in Fig. 2(a) is the HAADF image of the structure of the  $\text{Gd}_{2.25}\text{Ho}_{0.75}\text{IG}$  film. The dashed white lines in Figs. 2(a)–2(d) represent the sharp interface between the  $\text{Gd}_{3-x}\text{Ho}_x\text{IG}$  films and the GSGG substrates. In addition, the STEM experiment yields an accurate estimation of the film thickness of 13.7 nm. Figure 2(b) is the high-resolution HAADF image that is obtained within a selected area [yellow dashed line in Fig. 2(a)], in which a sharp interface without indication of defect and dislocation is evident. The spots with brighter contrasts denote the Gd or Ho atoms, which match well with the blue spheres plotted by the Visualization for Electronic and Structural Analysis (VESTA) software. The yellow (red) spheres are the d-Fe (a-Fe) atoms centered in oxygen tetrahedrons (octahedrons), respectively.

In addition, the random distribution of the Gd and Ho elements without clear evidence of segregation is also identified, as shown in Figs. 2(c) and 2(d), respectively. The corresponding distribution of Ga, Fe, and Sc are shown in Fig. S2(b) of the Supplemental Material (SM) [51] (also see Refs. [52–57]). Along the growth direction, estimations of the relative atomic fraction for  $x_{\text{Ho}} = 2.25, 1.5,$  and  $0.75$  films are

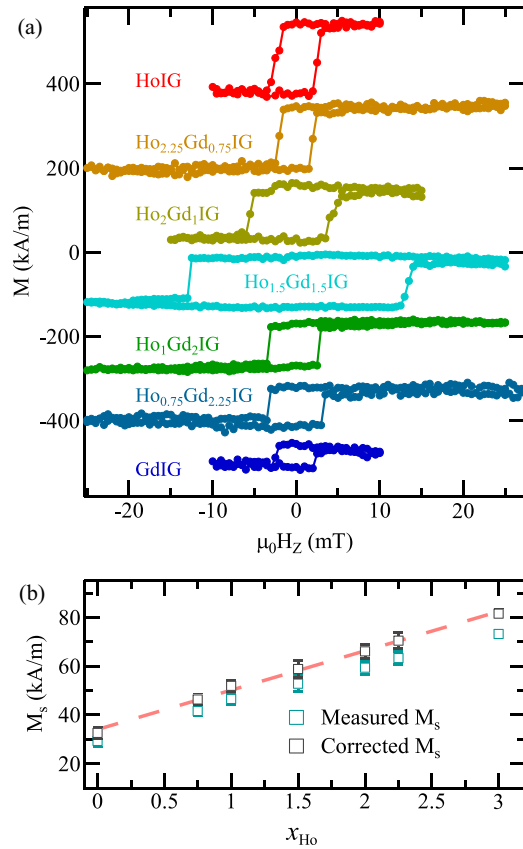


FIG. 3. (a) The perpendicular magnetic hysteresis loops ( $M - \mu_0 H_z$ ). (b) The evolution of the net saturation magnetization ( $M_s$ ) as a function of the Ho concentration ( $x_{\text{Ho}}$ ). The green dots represent the experimentally obtained magnetometry data, while the black dots represent the data after subtracting the influence of the magnetic dead layers, and the red dashed line is the linear fitting for corrected data.

shown in Figs. 2(e)–2(g), respectively. Note that the relative atomic fractions obtained from EDS mapping match with the estimated compositions based on the deposition rates, as discussed in Part 4 of the SM [51]. Furthermore, the relative atomic fractions across the interface for the  $x_{\text{Ho}} = 0.75$  film are shown in Fig. S2(c) of the SM [51]. The result of this reveals an interfacial region (around 1.7 nm) between the substrate and the  $\text{Gd}_{2.25}\text{Ho}_{0.75}\text{IG}$  film, in which the diffusion of Fe elements into the GSGG substrate can be found. This is similar to early studies [24,58–61].

### B. Part II: Continuous tuning of $M_s$ and $T_M$

Magnetic properties of the  $\text{Gd}_{3-x}\text{Ho}_x\text{IG}$  films were examined. After subtracting the linear paramagnetic background signal of the substrate, the square-shaped magnetic hysteresis loops ( $M - \mu_0 H_z$ ) that are measured under the out-of-plane geometry at room temperature confirm the presence of PMA, as shown in Fig. 3(a). Note that the thickness of the magnetic dead layer (MDL) is estimated as 1.4 nm. Its influence on the magnetic properties has been subtracted, as discussed in Part 8 of the SM [51]. The PMA agrees with the tensile strain in thin garnet films [10,15,21,22,36,48]. Note that coercive field

( $\mu_0 H_C$ ) varies nonmonotonically and reaches a maximum at  $x_{\text{Ho}} = 1.5$ , which could be attributed to the maximized atomic dissimilarity in the  $\text{Gd}_{1.5}\text{Ho}_{1.5}\text{IG}$  film. The evolution of the corrected  $M_s$  is summarized in Fig. 3(b), where  $M_s$  can be fitted by

$$M_s(x_{\text{Ho}}) = 34.1 + k_{M_s} x_{\text{Ho}}, \quad (2)$$

where  $M_s^{\text{GdIG}} \cong 34.1$  kA/m is the saturation magnetization of the GdIG film, and the slope is determined as  $k_{M_s} = (M_s^{\text{HoIG}} - M_s^{\text{GdIG}}) / x_{\text{Ho}} = 16.1$  kA/m. Such a linear dependence originates from the increased orbital magnetism of the substituted  $\text{Ho}^{3+}$  ions (with an electronic state of  $4f^{10}$ ).

As a result, a continuous tuning of the net saturation magnetization can be achieved in the  $\text{Gd}_{3-x}\text{Ho}_x\text{IG}$  films by precisely adjusting the Ho concentrations ( $x_{\text{Ho}}$ ). Note that the  $M_s$  value of 34 kA/m (81 kA/m) for GdIG (HoIG) thin films at room temperature is higher than the value of 8 kA/m (56 kA/m) in the bulk samples [2–4,50]. This could be attributed to the nonstoichiometry of commercial GdIG and HoIG targets. Moreover, the presence of this nonstoichiometry could lead to a lower compensation temperature ( $T_M$ ) in these thin films, as compared with the bulk materials, which will be discussed later [2–4].

In order to electrically detect the magnetization states of  $\text{Gd}_{3-x}\text{Ho}_x\text{IG}$  films, we employed the spin Hall induced anomalous Hall effect (SHAHE) via depositing a thin layer of heavy metal Pt [62–65]. An optical image of the Hall bar, together with the measurement geometry, is shown in the inset of Fig. 4(a). Shown in Fig. 4(a) are the square-shaped SHAHE loops ( $R_{xy}$  vs  $\mu_0 H_z$ ) from the  $\text{Gd}_2\text{Ho}_1\text{IG}/\text{Pt}$  bilayer. Note that the polarities of these SHAHE loops reverse their signs between 200 and 180 K, which suggests the net magnetization of the  $\text{Fe}^{3+}$  sublattices is fully compensated with those of the  $\text{Gd}^{3+}$  and  $\text{Ho}^{3+}$  sublattices [52,66]. Thus, a magnetization compensation temperature ( $T_M \approx 190$  K) can be approximately estimated. Note that  $T_M$  in the thin film is lower compared with the bulk samples, which could be related to the deficiency of the Re element. This is confirmed by the estimated ratio of the Fe content to the sum of the Gd and Ho content ( $\sim 1.77$ ), which deviates from the ideal value of 1.66, as shown in Fig S2(c) of the SM [51].

The perpendicular magnetic hysteresis loops ( $M - \mu_0 H_z$ ) at different temperatures for the same  $\text{Gd}_2\text{Ho}_1\text{IG}$  film are measured, as shown in Fig. 4(b). In the vicinity of  $T_M$ , a large coercive field ( $\mu_0 H_C$ ) and a vanishing hysteresis loop are shown by the gray-green dot in Fig. 4(b). Note that the coercive field measured from the Hall bar is higher compared with the continuous film. We attribute this phenomenon to the additional defects and pinning effects at the device edges introduced during the device fabrication process, which increase the domain nucleation field [19,23]. Summarized in Fig. 4(c) is the evolution of  $\mu_0 H_C$  as a function of temperature obtained from Fig. 4(a), which again diverges at  $T_M = 190$  K due to the strong antiferromagnetic coupling between the  $\text{Fe}^{3+}$  and  $\text{Gd}^{3+}/\text{Ho}^{3+}$  sublattices. The evolution of  $T_M$  as a function of  $x_{\text{Ho}}$  is presented in Fig. 4(e). Through a linear fitting, we get  $T_M(x_{\text{Ho}}) = 224.43 - k_{T_M} x_{\text{Ho}}$ , where  $T_M^{\text{GdIG}} = 224.04$  K is the estimated magnetization compensation temperature ( $T_M$ ) of the GdIG film and the slope of  $k_{T_M}$  is estimated to be 41 K. Note that  $T_M^{\text{GdIG}} = 224.04$  K is also consistent with

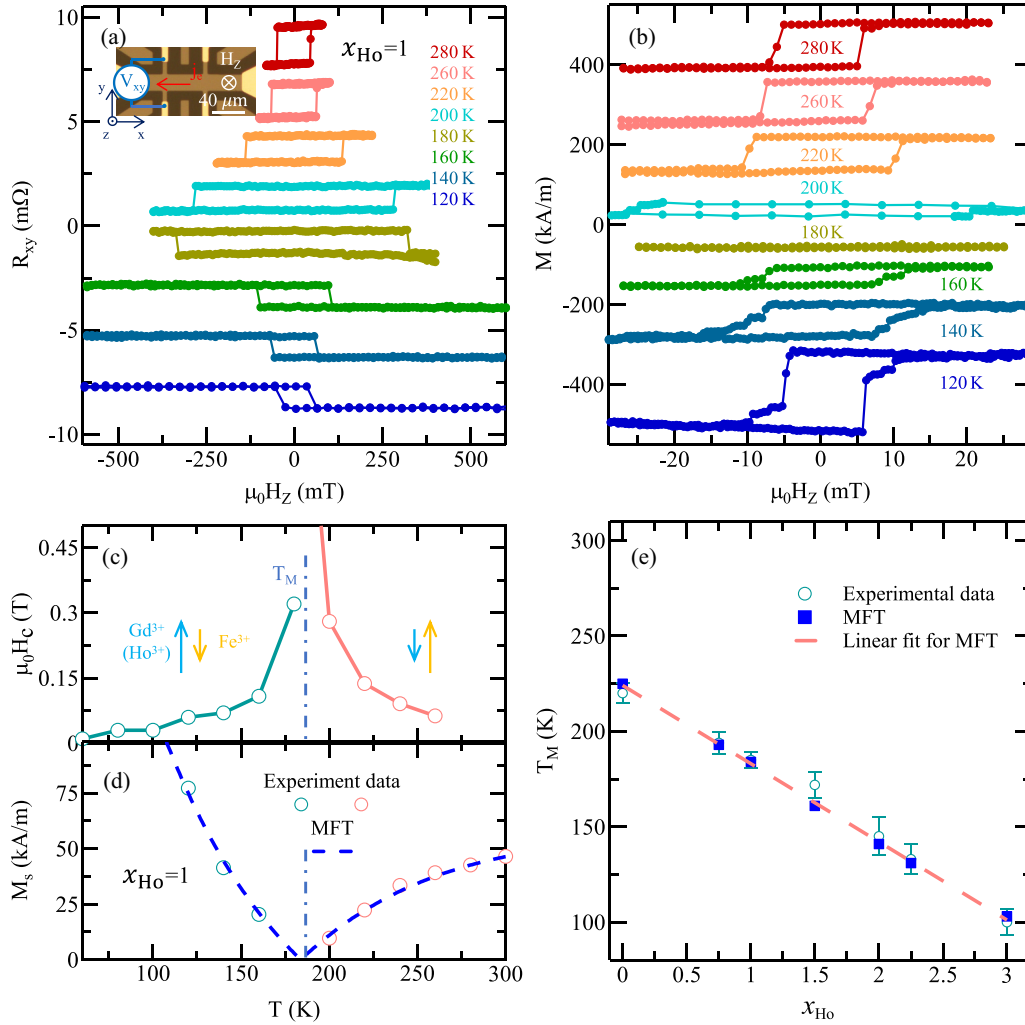


FIG. 4. (a) The SHAHE loops ( $R_{xy}$  vs  $\mu_0 H_z$ ) of the  $\text{Gd}_2\text{Ho}_1\text{IG}/\text{Pt}$  bilayers with temperatures ranging from 280 to 120 K. The inset illustrates an optical image of the Hall bar device, together with the SHAHE measurement geometry. (b) The perpendicular magnetic hysteresis loops ( $M - \mu_0 H_z$ ) were measured at different temperatures. (c) The evolution of coercive field ( $\mu_0 H_c$ ) as a function of temperature. The divergence at 190 K yields an estimation of the magnetization compensation temperature ( $T_M$ ). The yellow (blue) arrows represent the direction of magnetic moments of the  $\text{Fe}^{3+}$  and  $[\text{Re}^{3+} (\text{Gd}^{3+}, \text{Ho}^{3+})]$  sublattices above and below the compensation temperature ( $T_M$ ). (d) The corresponding temperature dependence of  $M_s$ , which also vanishes around 190 K. The light green (red) dots represent  $M_s$  measured below (above)  $T_M$ . The blue dashed line is the fitting line from the molecular-field model. (e) The evolution of  $T_M$  as a function of Ho concentrations ( $x_{\text{Ho}}$ ): the green dots are experimentally determined values, and the blue squares are the calculated results from the molecular-field theory. The red dashed line is the linear fitting of  $T_M$  against  $x_{\text{Ho}}$ .

our early results [43]. Shown in Fig. 4(d) is the corresponding temperature dependence of net saturation magnetization  $M_S$ , which also vanishes at  $T_M = 190$  K.

### C. Part III: Theory fit by the molecular-field model

Based on the molecular-field theory (MFT) [53,54,67], the temperature dependence of the net saturation magnetization [ $M_S(T)$ ] of these  $\text{Gd}_{3-x}\text{Ho}_x\text{IG}$  films can be decomposed as follows:

$$M_S(T) = M_a(T) + M_{\text{Gd}}(T) + M_{\text{Ho}}(T) - M_d(T), \quad (3)$$

where  $M_i(T) = M_i(0)B_{J_i}(x_i)$ , ( $i = a, d, \text{Gd}, \text{Ho}$ ) represents the temperature-dependent magnetization of different sublattices, and  $B_{J_i}(x_i)$  is the Brillouin function with  $x_i$  being a

temperature-sensitive function, which reads as

$$x_i = \left( \frac{J_i g_i \mu_B}{kT} \right) (N_{ia} M_a + N_{id} M_d + N_{i\text{Gd}} M_{\text{Gd}} + N_{i\text{Ho}} M_{\text{Ho}}). \quad (4)$$

Here  $J_i$  is the angular momentum and  $g_i$  is the Landé factor, and  $J_a = J_d = 5/2$ ,  $g_a = g_d = 2$  for  $\text{Fe}^{3+}$  sublattices;  $J_{\text{Gd}(\text{Ho})} = 7/2$  (8),  $g_{\text{Gd}(\text{Ho})} = 2$  (5/4) for  $\text{Gd}^{3+}$  ( $\text{Ho}^{3+}$ ) sublattices; and  $\mu_B$  is the Bohr magneton. Here  $N_{ij} = N_{ji}$ , ( $i, j = a, d, \text{Gd}, \text{Ho}$ ) are the molecular-field coefficients of different sublattices. Based on Dionne's model, the coefficients between a- $\text{Fe}^{3+}$  and d- $\text{Fe}^{3+}$  sublattices in different ReIGs read as  $N_{aa} = -65.0$ ,  $N_{dd} = -30.4$ ,  $N_{ad} = 97.0$ , in units of mole/cc [53,54]. The substitution of different c- $\text{Re}^{3+}$  sublattices leads to varied molecular-field coefficients with

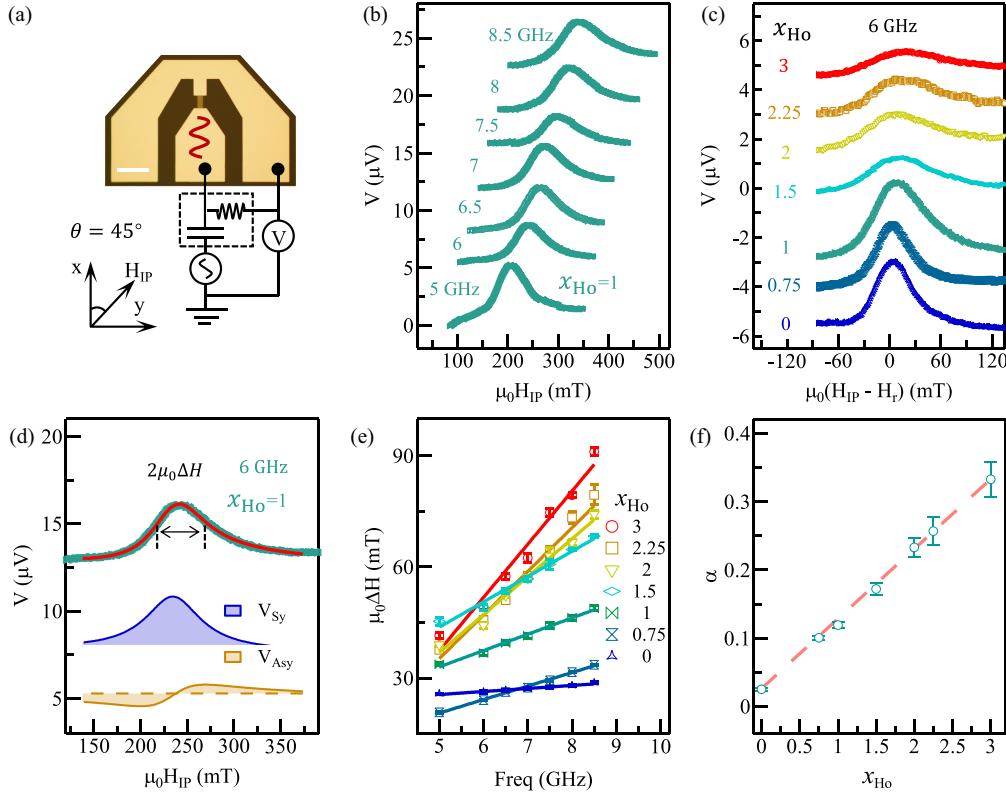


FIG. 5. (a) A schematic illustration of the STFM geometry; the scale bar is 100  $\mu\text{m}$ . (b) The typical FMR spectra in the  $\text{Gd}_2\text{Ho}_1\text{IG}/\text{Pt}$  bilayer with a nominal microwave 100 mW, at the microwave frequencies ranging from 5 to 8.5 GHz. (c) The FMR spectra at 6 GHz for all  $\text{Gd}_{3-x}\text{Ho}_x\text{IG}/\text{Pt}$  films ( $x_{\text{Ho}} = 0, 0.75, 1, 1.5, 2, 2.25, 3$ ). The decomposition of FMR spectra is shown in (d), where the light green line is the experimental data, and the red line corresponds to the fitting result. The blue (brown) line is the symmetric (asymmetric) line shape decomposed from the red line. (e) The evolution of linewidths ( $\mu_0\Delta H$ ) as a function of frequency ( $f$ ), a linear fitting of which yields an estimation of the damping parameter ( $\alpha$ ). (f) The evolution of damping parameter ( $\alpha$ ) as a function of the Ho concentration ( $x_{\text{Ho}}$ ), where the green dots are experimental data, and the red line represents the linear fitting result.

respect to those of the  $d\text{-Fe}^{3+}$  and  $a\text{-Fe}^{3+}$  sublattices, where  $N_{\text{aGd}} = -3.44$ ,  $N_{\text{aHo}} = -1.5$ , and  $N_{\text{dGd}} = 6.0$ ,  $N_{\text{dHo}} = 4.0$ , in units of mole/cc, respectively. At 0 K, the magnetization per formula unit is given by  $M_{\text{a}}(0) = 2J_{\text{a}}g_{\text{a}}\mu_{\text{B}}N$ ,  $M_{\text{d}}(0) = 3J_{\text{d}}g_{\text{d}}\mu_{\text{B}}N$ ,  $M_{\text{Gd}}(0) = 3t^*J_{\text{Gd}}g_{\text{Gd}}\mu_{\text{B}}N(1 - x_{\text{Ho}}/3)$ ,  $M_{\text{Ho}}(0) = 3J_{\text{Ho}}g_{\text{Ho}}\mu_{\text{B}}N(x_{\text{Ho}}/3)$ , with  $N$  being the Avogadro constant and  $t^*$  a normalization factor.

Based on this model, we will first examine the evolution of  $M_{\text{S}}(T)$  as a function of temperature in the  $\text{GdIG}$  ( $x_{\text{Ho}} = 0$ ) and  $\text{HoIG}$  ( $x_{\text{Ho}} = 3$ ) films, which is presented in Fig. S10 of the SM [51]. Here, a normalization factor  $t^* = 0.92$  is used as a result of nonstoichiometry of the  $\text{GdIG}$  film, which is estimated by the deficiency of elements from the EDS data and comparing the  $M_{\text{S}}$  and  $T_{\text{M}}$  of our films with that of the bulk samples [3,4,25]. We obtain the  $M_{\text{S}}(\text{GdIG}) = 13.62 \mu_{\text{B}}/\text{f.u.}$  and  $M_{\text{S}}(\text{HoIG}) = 8.81 \mu_{\text{B}}/\text{f.u.}$  at 0 K. A large deviation of  $M_{\text{S}}$  in the present  $\text{HoIG}$  films from that of the bulk sample [3,4,54] might be due to the canting effect arising from the lattice mismatch, which has been suggested in other  $\text{ReIGs}$  ( $\text{Re} = \text{Tb, Dy, Er, and Yb}$ ) [54].

Owing to the fixed magnetic moment and the molecular-field coefficients of the  $d\text{-Fe}^{3+}$  and  $a\text{-Fe}^{3+}$  sublattices in the  $\text{Gd}_{3-x}\text{Ho}_x\text{IG}$  films, we can formulate the temperature dependence of  $M_{\text{S}}(T)$  in the range of  $0 \leq x \leq 3$ . The blue

dashed line in Fig. 4(d) is the fitted result for the  $\text{Gd}_2\text{Ho}_1\text{IG}$  films, which agrees with the experimental data. Moreover, through changing the relative Ho compositions ( $x_{\text{Ho}}$ ), the estimated  $T_{\text{M}}$  from the MFT are consistent with the experimental data (black dots), shown as blue squares in Fig. 4(e). Given the compensated ferrimagnetism between  $\text{Gd}^{3+}(\text{Ho}^{3+})$  and  $\text{Fe}^{3+}$  sublattices, the very different Landé factors,  $g_{\text{Gd}(\text{Ho})} = 2$  ( $5/4$ ), should lead to a distinct difference between  $T_{\text{A}}$  and  $T_{\text{M}}$  in the  $\text{Gd}_{3-x}\text{Ho}_x\text{IG}$  films. This interesting aspect will be studied in the future.

#### D. Part IV: Linear evolution of Gilbert damping in the $\text{Gd}_{3-x}\text{Ho}_x\text{IG}$ films

To characterize the damping parameter of the  $\text{Gd}_{3-x}\text{Ho}_x\text{IG}/\text{Pt}$  bilayers at room temperature, the STFM spectra at different frequencies are obtained. It should be mentioned here that additional damping due to spin pumping effect could be introduced by using this technique. This measurement is conducted with an in-plane magnetic field ( $\mu_0 H_{\text{IP}}$ ) at an angle of  $45^\circ$  with respect to the RF current direction ( $x$  direction), as shown in Fig. 5(a). Shown in Fig. 5(b) are the typical FMR spectra that are obtained in the  $\text{Gd}_2\text{Ho}_1\text{IG}/\text{Pt}$  bilayer at room temperature, which

exhibit characteristic line shapes commonly observed in various other materials [55,68–74]. Following the increased microwave frequencies from 5 to 8.5 GHz, the resonance field ( $\mu_0 H_r$ ) shifts towards a higher field regime, and a resonance linewidth ( $\mu_0 \Delta H$ ) broadening is also observed. Similar experiments were conducted for all  $\text{Gd}_{3-x}\text{Ho}_x\text{IG}/\text{Pt}$  bilayers. Shown in Fig. 5(c) are the selected FMR spectra at 6 GHz. Following the increased Ho concentrations ( $x_{\text{Ho}}$ ), one can observe a gradually broadened linewidth ( $\mu_0 \Delta H$ ), which implies a gradually increased damping parameter.

Typical STFM voltage can be decomposed into a linear combination of symmetric ( $V_{\text{Sy}}$ ) and asymmetric ( $V_{\text{Asy}}$ ) components [56,57,75–77]. As a result, the STFM voltage can be well fitted, which can be seen from the solid red curve in Fig. 5(d). The fitting formula of STFM is presented in Part 14 of the SM [51]. Accordingly, the linewidth and the resonant field can be determined as  $\mu_0 \Delta H = 35.8$  mT and  $\mu_0 H_r = 234.5$  mT, respectively. Through extracting linewidths at different frequencies ( $f$ ), one can extrapolate the Gilbert damping parameter  $\alpha$  as follows:

$$\Delta H = \Delta H_0 + \frac{\alpha f}{\gamma_{\text{eff}}}, \quad (5)$$

where  $\Delta H_0$  arises from the inhomogeneous linewidth broadening, and  $\gamma_{\text{eff}}$  is the effective gyromagnetic ratio that is determined by the Kittel equation:  $f = |\gamma_{\text{eff}}| \mu_0 \sqrt{H_r(H_r - H_k)}$ .

Shown in Fig. 5(f) is the evolution of Gilbert damping parameter  $\alpha$  as a function of the Ho concentrations ( $x_{\text{Ho}}$ ). The value of  $\alpha$  increases monotonically following the increased  $x_{\text{Ho}}$  ( $0 \leq x_{\text{Ho}} \leq 3$ ), from  $0.025 \pm 0.002$  for the GdIG film and to  $0.333 \pm 0.026$  for the HoIG film. Such an evolution ( $\alpha - x_{\text{Ho}}$ ) can also be linearly fitted as follows:  $\alpha(x_{\text{Ho}}) = 0.025 + k_\alpha x_{\text{Ho}}$ , with the slope  $k_\alpha = 0.1023$ . Note that these damping parameters are also consistent with early works that were obtained in similar GdIG and HoIG films [44,78]. A larger Gilbert damping parameter in the HoIG film could be linked to the stronger SOC and the larger orbital momentum number  $L = 6$ , as compared with  $L = 0$  in the GdIG film. Thus, the increased SOC could introduce an additional source of energy dissipation, leading to levitated magnetic damping in ReIGs including LuIG [9], TmIG [11], DyIG [21], and EuIG [19].

Note that the value of  $\alpha$  in compensated ferrimagnets typically exhibits a strong temperature dependence, due to the strong temperature dependence of antiferromagnetic coupling between sublattices [44]. Shown in Part 16 of the SM [51] is the evolution of  $\alpha$  as a function of temperature for GdIG film, which diverges around 220 K and decreases as temperature deviates from the compensation temperatures. If antiferromagnetic coupling contributes dominantly to magnetic damping, one should observe a reduction of damping

parameters at room temperature, following the increased  $x_{\text{Ho}}$ . This could be attributed to the reduced  $T_M$  and  $T_A$ , as well as the reduced strength of antiferromagnetic coupling at room temperature, following the increased  $x_{\text{Ho}}$  [Fig. 4(e)]. Namely, the bigger deviation from the compensation temperature, the weaker the antiferromagnetic coupling. By contrast, our findings show an increase in  $\alpha$  with increasing  $x_{\text{Ho}}$  at room temperature, as shown in Fig. 5(f). More importantly, compared to the impact of temperature (which only leads to an increase of  $\alpha$  from 0.02 to 0.06), changes in  $x_{\text{Ho}}$  have a dominant effect on damping, increasing it by an order of magnitude (from 0.02 to 0.3). This observation indicates that the enhanced  $\alpha$  is dominated by the strong spin-orbit coupling (SOC) in  $\text{Ho}^{3+}$ .

#### IV. CONCLUSION

Using the cosputtering method, we have synthesized a series of  $\text{Gd}_{3-x}\text{Ho}_x\text{IG}$  films, in which the Ho concentration is continuously tuned ( $x_{\text{Ho}} = 0-3$ ). The high-quality growth is confirmed by morphological and structural characterizations. The presence of perpendicular magnetic anisotropy and its connection with the tensile strain provided by the mismatched substrate are also discussed. The evolution of magnetic properties as a function of the Ho concentration and temperature is also examined, which yields an estimation of the magnetization compensation temperature. By invoking the molecular-field theory, we can quantitatively characterize both the temperature-dependent and the Ho-concentration-dependent compensated ferrimagnetism. Meanwhile, a linear increase of the damping parameter is revealed, which is attributed to the increased spin-orbit coupling with the increased Ho concentration ( $x_{\text{Ho}}$ ). The Re substitution methods provide an effective approach for designing compensated garnets with desired magnetic properties, including the net saturation magnetization, the compensation temperature, and the magnetic damping parameters. Our results could be useful for designing functional spintronic materials based on compensated rare-earth iron garnets.

#### ACKNOWLEDGMENTS

Work carried out at Tsinghua was supported by the National Key R&D Program of China (Grant No. 2022YFA1405100), the Basic Science Center Project of National Natural Science Foundation of China (NSFC Grant No. 52388201), the NSFC general program (Grants No. 52271181 and No. 51831005), the distinguished Young Scholar program (Grant No. 12225409), Beijing Natural Science Foundation (Grant No. Z190009), Tsinghua University Initiative Scientific Research Program, and the Beijing Advanced Innovation Center for Future Chip (ICFC).

- 
- [1] F. Bertaut and F. Forrat, Structure des ferrites ferrimagnétiques des terres rares, C. R. Hebd. Seances Acad. Sci. **242**, 382 (1956).  
 [2] F. Bertaut and R. Pauthenet, Crystalline structure and magnetic properties of ferrites having the general formula

$5\text{Fe}_2\text{O}_3 \cdot 3\text{M}_2\text{O}_3$ , Proc. IEE - Part B: Radio Electron. Eng. **55**, 261 (1957).

- [3] R. Pauthenet, Spontaneous magnetization of some garnet ferrites and the aluminum substituted garnet ferrites, J. Appl. Phys. **29**, 253 (1958).

- [4] S. Geller, J. P. Remeika, R. C. Sherwood, H. J. Williams, and G. P. Espinosa, Magnetic study of the heavier rare-earth iron garnets, *Phys. Rev.* **137**, A1034 (1965).
- [5] N. Kumar, N. G. Kim, Y. A. Park, N. Hur, J. H. Jung, K. J. Han, and K. J. Yee, Epitaxial growth of terbium iron garnet thin films with out-of-plane axis of magnetization, *Thin Solid Films* **516**, 7753 (2008).
- [6] M. C. Onbasli, A. Kehlberger, D. H. Kim, G. Jakob, M. Kläui, A. V. Chumak, B. Hillebrands, and C. A. Ross, Pulsed laser deposition of epitaxial yttrium iron garnet films with low Gilbert damping and bulk-like magnetization, *APL Mater.* **2**, 106102 (2014).
- [7] H. Chang, P. Li, W. Zhang, T. Liu, A. Hoffmann, L. Deng, and M. Wu, Nanometer-thick yttrium iron garnet films with extremely low damping, *IEEE Magn. Lett.* **5**, 1 (2014).
- [8] M. B. Jungfleisch, A. V. Chumak, A. Kehlberger, V. Lauer, D. H. Kim, M. C. Onbasli, C. A. Ross, M. Kläui, and B. Hillebrands, Thickness and power dependence of the spin-pumping effect in  $\text{Y}_3\text{Fe}_5\text{O}_{12}/\text{Pt}$  heterostructures measured by the inverse spin Hall effect, *Phys. Rev. B* **91**, 134407 (2015).
- [9] C. L. Jermain, H. Paik, S. V. Aradhya, R. A. Buhrman, D. G. Schlom, and D. C. Ralph, Low-damping sub-10-nm thin films of lutetium iron garnet grown by molecular-beam epitaxy, *Appl. Phys. Lett.* **109**, 192408 (2016).
- [10] L. Soumah, N. Beaulieu, L. Qassym, C. Carrétéro, E. Jacquet, R. Lebourgeois, J. Ben Youssef, P. Bortolotti, V. Cros, and A. Anane, Ultra-low damping insulating magnetic thin films get perpendicular, *Nat. Commun.* **9**, 3355 (2018).
- [11] S. Crossley, A. Quindeau, A. G. Swartz, E. R. Rosenberg, L. Beran, C. O. Avci, Y. Hikita, C. A. Ross, and H. Y. Hwang, Ferromagnetic resonance of perpendicularly magnetized  $\text{Tm}_3\text{Fe}_5\text{O}_{12}/\text{Pt}$  heterostructures, *Appl. Phys. Lett.* **115**, 172402 (2019).
- [12] L. J. Cornelissen, J. Liu, R. A. Duine, J. Ben Youssef, and B. J. van Wees, Long-distance transport of magnon spin information in a magnetic insulator at room temperature, *Nat. Phys.* **11**, 1022 (2015).
- [13] X. Y. Wei, O. A. Santos, C. H. S. Lusero, G. E. W. Bauer, J. Ben Youssef, and B. J. van Wees, Giant magnon spin conductivity in ultrathin yttrium iron garnet films, *Nat. Mater.* **21**, 1352 (2022).
- [14] H. Yamahara, M. Mikami, M. Seki, and H. Tabata, Epitaxial strain-induced magnetic anisotropy in  $\text{Sm}_3\text{Fe}_5\text{O}_{12}$  thin films grown by pulsed laser deposition, *J. Magn. Magn. Mater.* **323**, 3143 (2011).
- [15] C. Tang, P. Sellappan, Y. Liu, Y. Xu, J. E. Garay, and J. Shi, Anomalous Hall hysteresis in  $\text{Tm}_3\text{Fe}_5\text{O}_{12}/\text{Pt}$  with strain-induced perpendicular magnetic anisotropy, *Phys. Rev. B* **94**, 140403(R) (2016).
- [16] J. B. Fu, M. X. Hua, X. Wen, M. Z. Xue, S. L. Ding, M. Wang, P. Yu, S. Q. Liu, J. Z. Han, C. S. Wang *et al.*, Epitaxial growth of  $\text{Y}_3\text{Fe}_5\text{O}_{12}$  thin films with perpendicular magnetic anisotropy, *Appl. Phys. Lett.* **110**, 202403 (2017).
- [17] A. Quindeau, C. O. Avci, W. Liu, C. Sun, M. Mann, A. S. Tang, M. C. Onbasli, D. Bono, P. M. Voyles, Y. Xu *et al.*,  $\text{Tm}_3\text{Fe}_5\text{O}_{12}/\text{Pt}$  heterostructures with perpendicular magnetic anisotropy for spintronic applications, *Adv. Electron. Mater.* **3**, 1600376 (2017).
- [18] Y. K. Liu, H. F. Wong, K. K. Lam, K. H. Chan, C. L. Mak, and C. W. Leung, Anomalous Hall effect in  $\text{Pt}/\text{Tb}_3\text{Fe}_5\text{O}_{12}$  heterostructure: Effect of compensation point, *J. Magn. Magn. Mater.* **468**, 235 (2018).
- [19] E. R. Rosenberg, L. Beran, C. O. Avci, C. Zeledon, B. Song, C. Gonzalez-Fuentes, J. Mendil, P. Gambardella, M. Veis, C. Garcia *et al.*, Magnetism and spin transport in rare-earth-rich epitaxial terbium and europium iron garnet films, *Phys. Rev. Mater.* **2**, 094405 (2018).
- [20] J. J. Bauer, E. R. Rosenberg, and C. A. Ross, Perpendicular magnetic anisotropy and spin mixing conductance in polycrystalline europium iron garnet thin films, *Appl. Phys. Lett.* **114**, 052403 (2019).
- [21] J. J. Bauer, E. R. Rosenberg, S. Kundu, K. A. Mkhoyan, P. Quarterman, A. J. Grutter, B. J. Kirby, J. A. Borchers, and C. A. Ross, Dysprosium iron garnet thin films with perpendicular magnetic anisotropy on silicon, *Adv. Electron. Mater.* **6**, 1900820 (2020).
- [22] S. Mokarian Zanjani and M. C. Onbaşlı, Predicting new iron garnet thin films with perpendicular magnetic anisotropy, *J. Magn. Magn. Mater.* **499**, 166108 (2020).
- [23] C. O. Avci, A. Quindeau, C. F. Pai, M. Mann, L. Caretta, A. S. Tang, M. C. Onbasli, C. A. Ross, and G. S. Beach, Current-induced switching in a magnetic insulator, *Nat. Mater.* **16**, 309 (2017).
- [24] Q. Shao, C. Tang, G. Yu, A. Navabi, H. Wu, C. He, J. Li, P. Upadhyaya, P. Zhang, S. A. Razavi *et al.*, Role of dimensional crossover on spin-orbit torque efficiency in magnetic insulator thin films, *Nat. Commun.* **9**, 3612 (2018).
- [25] J. Hanton, Intrinsic coercive force of rare earth iron garnets near the compensation temperature, *IEEE Trans. Magn.* **3**, 505 (1967).
- [26] C. D. Mee, The magnetization mechanism in single-crystal garnet slabs near the compensation temperature, *IBM J. Res. Dev.* **11**, 468 (1967).
- [27] W. K. Liu, B. Cheng, S. Q. Ren, W. Huang, J. H. Xie, G. J. Zhou, H. W. Qin, and J. F. Hu, Thermally assisted magnetization control and switching of  $\text{Dy}_3\text{Fe}_5\text{O}_{12}$  and  $\text{Tb}_3\text{Fe}_5\text{O}_{12}$  ferrimagnetic garnet by low density current, *J. Magn. Magn. Mater.* **507**, 166804 (2020).
- [28] L. Liu, Z. Q. Fan, Z. R. Chen, Z. H. Chen, Z. X. Ye, H. N. Zheng, Q. Zeng, W. Jia, S. Q. Li, N. Wang *et al.*, Spin-orbit torques in heavy metal/ferrimagnetic insulator bilayers near compensation, *Appl. Phys. Lett.* **119**, 052401 (2021).
- [29] Z. Ren, K. Qian, M. Aldosary, Y. Liu, S. K. Cheung, I. Ng, J. Shi, and Q. Shao, Strongly heat-assisted spin-orbit torque switching of a ferrimagnetic insulator, *APL Mater.* **9**, 051117 (2021).
- [30] Y. Li, D. Zheng, C. Liu, C. Zhang, B. Fang, A. Chen, Y. Ma, A. Manchon, and X. Zhang, Current-induced magnetization switching across a nearly room-temperature compensation point in an insulating compensated ferrimagnet, *ACS Nano* **16**, 8181 (2022).
- [31] L. Caretta, S. H. Oh, T. Fakhru, D. K. Lee, B. H. Lee, S. K. Kim, C. A. Ross, K. J. Lee, and G. S. D. Beach, Relativistic kinematics of a magnetic soliton, *Science* **370**, 1438 (2020).
- [32] H.-A. Zhou, Y. Dong, T. Xu, K. Xu, L. Sánchez-Tejerina, L. Zhao, Y. Ba, P. Gargiani, M. Valvidares, Y. Zhao, M. Carpentieri, O. A. Tretiakov, X. Zhong, G. Finocchio, S. K. Kim, and W. Jiang, Compensated magnetic insulators for extremely fast spin-orbitronics, [arXiv:1912.01775](https://arxiv.org/abs/1912.01775).



- [33] J. Finley and L. Liu, Spin-Orbit-Torque Efficiency in Compensated Ferrimagnetic Cobalt-Terbium Alloys, *Phys. Rev. Appl.* **6**, 054001 (2016).
- [34] R. Mishra, J. Yu, X. Qiu, M. Motapothula, T. Venkatesan, and H. Yang, Anomalous Current-Induced Spin Torques in Ferrimagnets Near Compensation, *Phys. Rev. Lett.* **118**, 167201 (2017).
- [35] K.-J. Kim, S. K. Kim, Y. Hirata, S.-H. Oh, T. Tono, D.-H. Kim, T. Okuno, W. S. Ham, S. Kim, and G. Go, Fast domain wall motion in the vicinity of the angular momentum compensation temperature of ferrimagnets, *Nat. Mater.* **16**, 1187 (2017).
- [36] L. Caretta, M. Mann, F. Büttner, K. Ueda, B. Pfau, C. M. Günther, P. Hessing, A. Churikova, C. Klose, M. Schneider *et al.*, Fast current-driven domain walls and small skyrmions in a compensated ferrimagnet, *Nat. Nanotechnol.* **13**, 1154 (2018).
- [37] S. A. Siddiqui, J. Han, J. T. Finley, C. A. Ross, and L. Liu, Current-Induced Domain Wall Motion in a Compensated Ferrimagnet, *Phys. Rev. Lett.* **121**, 057701 (2018).
- [38] H. Wu, Y. Xu, P. Deng, Q. Pan, S. A. Razavi, K. Wong, L. Huang, B. Dai, Q. Shao, G. Yu *et al.*, Spin-Orbit torque switching of a nearly compensated ferrimagnet by topological surface states, *Adv. Mater.* **31**, 1901681 (2019).
- [39] K. Cai, Z. Zhu, J. M. Lee, R. Mishra, L. Ren, S. D. Pollard, P. He, G. Liang, K. L. Teo, and H. Yang, Ultrafast and energy-efficient spin-orbit torque switching in compensated ferrimagnets, *Nat. Electron.* **3**, 37 (2020).
- [40] J. Finley and L. Liu, Spintronics with compensated ferrimagnets, *Appl. Phys. Lett.* **116**, 110501 (2020).
- [41] S. K. Kim, G. S. D. Beach, K.-J. Lee, T. Ono, T. Rasing, and H. Yang, Ferrimagnetic spintronics, *Nat. Mater.* **21**, 24 (2022).
- [42] M. Uemura, T. Yamagishi, S. Ebisu, S. Chikazawa, and S. Nagata, A double peak of the coercive force near the compensation temperature in the rare earth iron garnets, *Philos. Mag.* **88**, 209 (2008).
- [43] H.-A. Zhou, L. Cai, T. Xu, Y. Zhao, and W. Jiang, Optimized growth of compensated ferrimagnetic insulator  $Gd_3Fe_5O_{12}$  with a perpendicular magnetic anisotropy, *Chin. Phys. B* **30**, 097503 (2021).
- [44] Y. Li, D. Zheng, B. Fang, C. Liu, C. Zhang, A. Chen, Y. Ma, K. Shen, H. Liu, A. Manchon *et al.*, Unconventional spin pumping and magnetic damping in an insulating compensated ferrimagnet, *Adv. Mater.* **34**, 2200019 (2022).
- [45] S. Geprägs, A. Kehlberger, F. D. Coletta, Z. Qiu, E.-J. Guo, T. Schulz, C. Mix, S. Meyer, A. Kamra, M. Althammer *et al.*, Origin of the spin Seebeck effect in compensated ferrimagnets, *Nat. Commun.* **7**, 10452 (2016).
- [46] H. Bai, Z. Z. Zhu, X. Z. Zhan, M. Yang, G. Li, J. T. Ke, C. Q. Hu, T. Zhu, and J. W. Cai, Polarized neutron reflectometry characterization of perpendicular magnetized  $Ho_3Fe_5O_{12}$  films with efficient spin-orbit torque induced switching, *Appl. Phys. Lett.* **119**, 212406 (2021).
- [47] M. Kubota, K. Shibuya, Y. Tokunaga, F. Kagawa, A. Tsukazaki, Y. Tokura, and M. Kawasaki, Systematic control of stress-induced anisotropy in pseudomorphic iron garnet thin films, *J. Magn. Magn. Mater.* **339**, 63 (2013).
- [48] C. Y. Guo, C. H. Wan, M. K. Zhao, H. Wu, C. Fang, Z. R. Yan, J. F. Feng, H. F. Liu, and X. F. Han, Spin-orbit torque switching in perpendicular  $Y_3Fe_5O_{12}/Pt$  bilayer, *Appl. Phys. Lett.* **114**, 192409 (2019).
- [49] J. Weidenborner, Least squares refinement of the structure of gadolinium-iron garnet  $Gd_3Fe_2Fe_3O_{12}$ , *Acta Crystallogr.* **14**, 1051 (1961).
- [50] R. Nakamoto, B. Xu, C. Xu, H. Xu, and L. Bellaiche, Properties of rare-earth iron garnets from first principles, *Phys. Rev. B* **95**, 024434 (2017).
- [51] See Supplemental Material at <http://link.aps.org/supplemental/10.1103/PhysRevMaterials.7.094401> for the STEM image and EDS mapping of the samples; the comparison between xHo obtained from EDS and sputtering rates; the weight fractions for samples; the determination of the thickness of the magnetic dead layer; the molecular-field coefficients used in the main text; the comparison between the influences of temperature and Ho compositions on the Gilbert damping. The Supplemental Material also contains Refs. [52–57].
- [52] T. Shirakawa, Y. Nakajima, K. Okamoto, S. Matsushita, and Y. Sakurai, The Kerr and the Hall effects in amorphous magnetic films, in *Magnetism and Magnetic Materials–1976: Proceedings of the First Joint MMM-Intermag Conference*, AIP Conf. Proc. No. 34 (AIP, Melville, NY, 1976), p. 349.
- [53] G. F. Dionne, Molecular field and exchange constants of  $Gd^{3+}$ -substituted ferrimagnetic garnets, *J. Appl. Phys.* **42**, 2142 (1971).
- [54] G. F. Dionne, Molecular-field coefficients of rare-earth iron garnets, *J. Appl. Phys.* **47**, 4220 (1976).
- [55] B. Heinrich, C. Burrowes, E. Montoya, B. Kardasz, E. Girt, Y.-Y. Song, Y. Sun, and M. Wu, Spin Pumping at the Magnetic Insulator (YIG)/Normal Metal (Au) Interfaces, *Phys. Rev. Lett.* **107**, 066604 (2011).
- [56] L. Liu, T. Moriyama, D. C. Ralph, and R. A. Buhrman, Spin-Torque Ferromagnetic Resonance Induced by the Spin Hall Effect, *Phys. Rev. Lett.* **106**, 036601 (2011).
- [57] M. Harder, Z. X. Cao, Y. S. Gui, X. L. Fan, and C. M. Hu, Analysis of the line shape of electrically detected ferromagnetic resonance, *Phys. Rev. B* **84**, 054423 (2011).
- [58] J. F. K. Cooper, C. J. Kinane, S. Langridge, M. Ali, B. J. Hickey, T. Niizeki, K. Uchida, E. Saitoh, H. Ambaye, and A. Glavic, Unexpected structural and magnetic depth dependence of YIG thin films, *Phys. Rev. B* **96**, 104404 (2017).
- [59] A. Mitra, O. Cespedes, Q. Ramasse, M. Ali, S. Marmion, M. Ward, R. M. D. Brydson, C. J. Kinane, J. F. K. Cooper S. Langridge *et al.*, Interfacial origin of the magnetisation suppression of thin film yttrium iron Garnet, *Sci. Rep.* **7**, 11774 (2017).
- [60] S. M. Sutin, A. M. Korovin, V. E. Bursian, L. V. Lutsev, V. Bourobina, N. L. Yakovlev, M. Montecchi, L. Pasquali, V. Ukleev, A. Vorobiev *et al.*, Role of gallium diffusion in the formation of a magnetically dead layer at the  $Y_3Fe_5O_{12}/Gd_3Fe_5O_{12}$  epitaxial interface, *Phys. Rev. Mater.* **2**, 104404 (2018).
- [61] L. Caretta, E. Rosenberg, F. Büttner, T. Fakhrlul, P. Gargiani, M. Valvidares, Z. Chen, P. Reddy, D. A. Muller, C. A. Ross *et al.*, Interfacial Dzyaloshinskii-Moriya interaction arising from rare-earth orbital magnetism in insulating magnetic oxides, *Nat. Commun.* **11**, 1090 (2020).
- [62] Y. T. Chen, S. Takahashi, H. Nakayama, M. Althammer, S. T. B. Goennenwein, E. Saitoh, and G. E. W. Bauer, Theory of spin Hall magnetoresistance, *Phys. Rev. B* **87**, 144411 (2013).
- [63] C. Hahn, G. de Loubens, O. Klein, M. Viret, V. V. Naletov, and J. Ben Youssef, Comparative measurements of inverse

- spin Hall effects and magnetoresistance in YIG/Pt and YIG/Ta, *Phys. Rev. B* **87**, 174417 (2013).
- [64] N. Vlietstra, J. Shan, V. Castel, B. J. van Wees, and J. Ben Youssef, Spin-Hall magnetoresistance in platinum on yttrium iron garnet: Dependence on platinum thickness and in-plane/out-of-plane magnetization, *Phys. Rev. B* **87**, 184421 (2013).
- [65] S. Meyer, R. Schlitz, S. Geprägs, M. Opel, H. Huebl, R. Gross, and S. T. B. Goennenwein, Anomalous Hall effect in YIG/Pt bilayers, *Appl. Phys. Lett.* **106**, 132402 (2015).
- [66] Y. Mimura, N. Imamura, and Y. Kushiro, Hall effect in rare-earth-transition-metal amorphous alloy films, *J. Appl. Phys.* **47**, 3371 (1976).
- [67] E. E. Anderson, Molecular field model and the magnetization of YIG, *Phys. Rev.* **134**, A1581 (1964).
- [68] J. E. Hirsch, Spin Hall Effect, *Phys. Rev. Lett.* **83**, 1834 (1999).
- [69] Y. Tserkovnyak, A. Brataas, G. E. W. Bauer, and B. I. Halperin, Nonlocal magnetization dynamics in ferromagnetic heterostructures, *Rev. Mod. Phys.* **77**, 1375 (2005).
- [70] E. Saitoh, M. Ueda, H. Miyajima, and G. Tatara, Conversion of spin current into charge current at room temperature: Inverse spin-Hall effect, *Appl. Phys. Lett.* **88**, 182509 (2006).
- [71] K. Uchida, S. Takahashi, K. Harii, J. Ieda, W. Koshibae, K. Ando, S. Maekawa, and E. Saitoh, Observation of the spin Seebeck effect, *Nature (London)* **455**, 778 (2008).
- [72] T. Chiba, G. E. W. Bauer, and S. Takahashi, Current-Induced Spin-Torque Resonance of Magnetic Insulators, *Phys. Rev. Appl.* **2**, 034003 (2014).
- [73] H. Zhou, X. Fan, L. Ma, Q. Zhang, L. Cui, S. Zhou, Y. S. Gui, C. M. Hu, and D. Xue, Spatial symmetry of spin pumping and inverse spin Hall effect in the Pt/Y<sub>3</sub>Fe<sub>5</sub>O<sub>12</sub> system, *Phys. Rev. B* **94**, 134421 (2016).
- [74] M. B. Jungfleisch, W. Zhang, J. Sklenar, J. Ding, W. Jiang, H. Chang, F. Y. Fradin, J. E. Pearson, J. B. Ketterson, V. Novosad *et al.*, Large Spin-Wave Bullet in a Ferrimagnetic Insulator Driven by the Spin Hall Effect, *Phys. Rev. Lett.* **116**, 057601 (2016).
- [75] L. Bai, P. Hyde, Y. S. Gui, C. M. Hu, V. Vlaminc, J. E. Pearson, S. D. Bader, and A. Hoffmann, Universal Method for Separating Spin Pumping from Spin Rectification Voltage of Ferromagnetic Resonance, *Phys. Rev. Lett.* **111**, 217602 (2013).
- [76] R. Iguchi, K. Sato, D. Hirobe, S. Daimon, and E. Saitoh, Effect of spin Hall magnetoresistance on spin pumping measurements in insulating magnet/metal systems, *Appl. Phys. Express* **7**, 013003 (2014).
- [77] P. Wang, S. W. Jiang, Z. Z. Luan, L. F. Zhou, H. F. Ding, Y. Zhou, X. D. Tao, and D. Wu, Spin rectification induced by spin Hall magnetoresistance at room temperature, *Appl. Phys. Lett.* **109**, 112406 (2016).
- [78] H. Bai, Z. Z. Zhu, J. T. Ke, G. Li, J. Su, Y. Zhang, T. Zhu, and J. W. Cai, Large Tunable Perpendicular Magnetic Anisotropy in Y<sub>3-x</sub>Tm<sub>x</sub>Fe<sub>5</sub>O<sub>12</sub> ( $x = 0-3$ ) Epitaxial Films with Minor Changes in Switching Current, *Phys. Rev. Appl.* **17**, 064023 (2022).